Nuclear Science and Techniques (2026) 37:36
https://doi.org/10.1007/s41365-025-01848-4

Candidate injector design for the Southern Advanced Photon Source based on linac and booster

Liang-Sheng Huang[1,2] · **Yan-Liang Han**[1,2] · **Wei-Hang Liu**[1,2] · **Jian-Liang Chen**[1,2] · **Sheng Wang**[1,2] · **Yi Jiao**[1,2] · **Xiao Li**[1,2] · **Jia-Xin Chen**[1,2]

Received: 15 July 2024 / Revised: 14 September 2024 / Accepted: 16 October 2024 / Published online: 5 January 2026

Abstract

The Southern Advanced Photon Source (SAPS) is a diffraction-limited synchrotron light source under design, which employs longitudinal injection as its primary injection scheme. This kind of injection scheme requires that the injected beam has a short bunch length and low emittance, and the preferred injector should offer high stability and low cost. Therefore, an injector based on a booster synchrotron was developed. The proposed injector includes a 250 MeV linac, a booster synchrotron that ramps the beam energy to 3.5 GeV, and two beam transport lines to ensure efficient beam delivery and beam quality preservation. The linac utilizes a thermionic high-voltage DC gun for reliable operation and features a bunching system with an advanced focusing system to preserve the emittance. To meet the injection requirements of the SAPS, a comprehensive design for the booster has been conducted. The booster synchrotron employs a threefold lattice structure, incorporating modified theoretical minimum emittance cells with a small momentum compaction factor and a high voltage to achieve an emittance of 3.98 nm rad and a bunch length of 4.8 mm. The injector has the potential to deliver a high charge, reducing the injection period of the storage ring to less than 1 min. Simulations demonstrated the expected performance, with a transmission efficiency of 90%, confirming its capability to meet the injection requirement of the SAPS storage ring. This design offers a stable and efficient solution for the SAPS.

Keywords Southern Advanced Photon Source · Longitudinal injection · Booster synchrotron · Emittance · Bunch length

1 Introduction

Diffraction-limited storage rings (DLSRs) represent a new generation of storage-ring-based light sources, designed to deliver high-brightness synchrotron radiation by minimizing beam emittance to approach the diffraction limit of X-rays. The MAX-IV [1, 2] is the first diffraction-limited light source. Subsequently, many DLSRs [3–15] have been launched around the world. To achieve ultra-low beam emittance within a reasonable circumference, the design of a DLSR typically incorporates a multi-bend achromat (MBA) [16] lattice with a small dynamic aperture. Alternative injection schemes [17–26] with relaxed dynamic aperture requirements have been extensively explored, particularly novel on-axis injection schemes [19–26]. Those approaches require a dynamic aperture only a few times larger than the injected beam size. One such on-axial injection is swap out injection [19], and it has been implemented by several DLSRs [20–22]. Another on-axis injection option is longitudinal novel injection [23–26]. In these schemes,

---

Liang-Sheng Huang, Yan-Liang Han have contributed equally to this work.

This work was supported by the Guangdong Basic and Applied Basic Research Foundation, China (No. 2021B1515140007).

✉ Yi Jiao
jiaoyi@ihep.ac.cn

✉ Xiao Li
lixiao@ihep.ac.cn

[1] Key Laboratory of Particle Acceleration Physics and Technology, Institute of High Energy Physics, CAS, Beijing 100049, China

[2] Spallation Neutron Source Science Center, Dongguan 523803, China

the bunch is injected on-axis transversely but with an energy and/or phase deviation relative to the synchronous particles. Longitudinal injection requires superior performance in beam dynamics to accommodate the oscillations of the injected beam, including low emittance and very short bunch lengths. The horizontal natural emittance of an electron beam in a ring can be written as [27]

$$\epsilon = C_q F(\text{type}) \frac{\gamma^2}{J_x N_\text{b}^3}, \tag{1}$$

where $C_q = 3.83 \times 10^{-13}$ m, γ is the Lorentz factor with speed light c, J_x is damping partition number in horizontal plane. F(type) is a dimensionless quantity that depends on the lattice type. For example, F is $1/(12\sqrt{15})$ for a theoretical minimum emittance (TME) unit cell. Furthermore, N_b denotes the number of bending magnets and increasing N_b effectively decreases emittance. To a certain extent, increasing N_b is equivalent to enlarging the ring circumference. The root-mean-square (RMS) bunch length σ_L is given [28] as

$$\sigma_\text{L} = \sqrt{\frac{\alpha_\text{p}}{2\pi heVE|\cos\phi_\text{s}|}} C\sigma_E, \tag{2}$$

where σ_E is the RMS energy spread, e is the electric charge, α_p is the momentum compaction factor with the ring circumference C, h is the harmonic number. V is the cavity voltage with synchronous phase ϕ_s. It is clear that increasing the voltage, reducing the circumference and lowering α_p can decrease bunch length. Considering the bunch length and emittance, reducing α_p becomes the primary optimization option in the lattice design.

The growing demand for a high-performance synchrotron light source in southern China has led to the proposal of the Southern Advanced Photon Source (SAPS) [29–31]. The SAPS is a 3.5 GeV DLSR light source planned for construction near the China Spallation Neutron Source (CSNS) facility [32]. Together with the CSNS, this new light source is expected to significantly enhance multidisciplinary scientific research in Southern China. The current storage ring of the SAPS spans 810 m, provides an emittance of 26 pm rad and supports a beam current of 500 mA. To enhance the stability of light, the SAPS employs longitudinal injection as the primary injection scheme [33]. For the injector system, several candidate options have been considered, including a full-energy linac injector [34] and a booster-based injector. The preference for the booster-based injector arises from its utilization of highly stable and thoroughly validated conventional magnets and acceleration units, which offer superior stability and minimize instrumentation expenses. To further improve the stability and operational efficiency of the light sources, many boosters implement separate tunnel with the storage ring [35–52]. This strategy has also been suggested for the SAPS. Figure 1 presents key accelerator parameters worldwide where boosters with separate tunnels are employed [35–48, 51]. These parameters include the circumference of the storage ring, booster energy, emittance and bunch length in relation to the booster circumference.

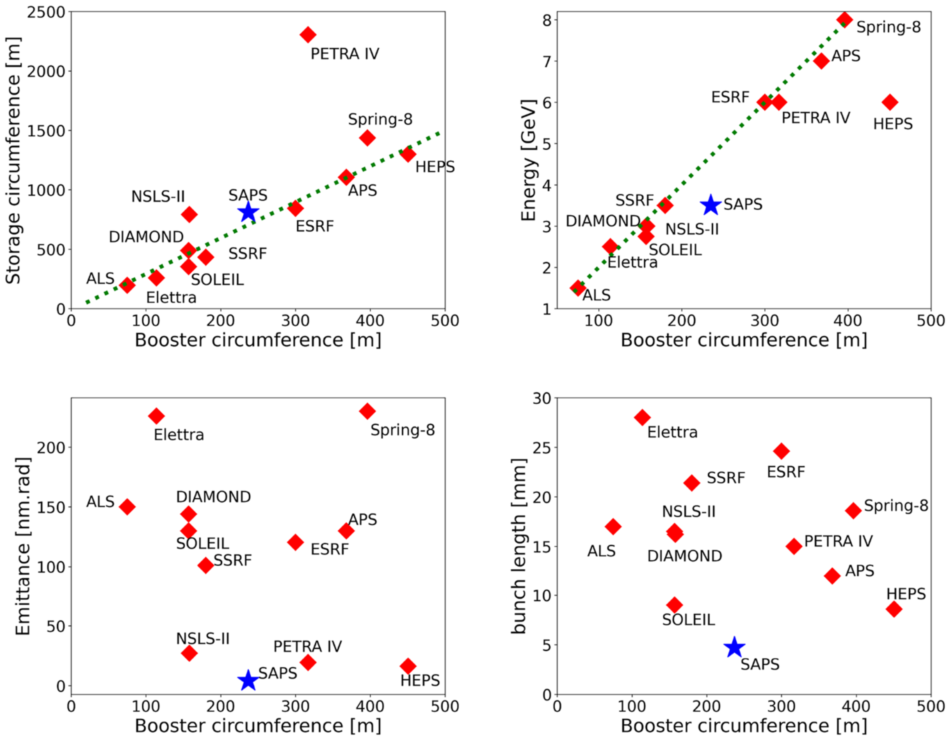

Fig. 1 (Color online) The key parameters of boosters with separate tunnels, employed as injectors in light sources globally. The upper left plot illustrates the relationship between the circumferences of the storage ring and the booster, with a ratio of 3:1 (dotted line). The upper right plot depicts the booster energy, showing a ratio of 2 GeV per 100 meters (dotted line). The lower left and right plots display the beam emittance and bunch length relative to the booster's circumference. The designed emittance of 3.98 nm rad and the bunch length of 4.8 mm are used for the SAPS booster. Due to publication limitations, the bunch length parameters for certain boosters are approximated values

Specifically, the upper left plot illustrates the relationship between the circumferences, with most light sources exhibiting a ratio of approximately 3:1. The upper right plot summarizes booster acceleration energy, indicating an increase of roughly 2 GeV for every 100 m of circumference. The emittance and bunch length in terms of the circumference are not clearly depicted in the lower sides of Fig. 1. Nevertheless, these plots highlight the significant advantages of the beam performance in the SAPS booster.

To fulfill the requirements for beam quality and efficiency in top-up operation modes of the storage ring, the booster-based injector should deliver electron bunches with high beam quality, as summarized in Ref. [53] and outlined in Table 1. With a bunch spacing of 6 ns in the storage ring, the longitudinal injection must be precisely executed within this 6-ns period. To prevent disturbances to the circulating beam during injection and reduce the difficulty of injection kickers, the injection phase is very close to the unstable phase of the bucket, which imposes significant constraints on longitudinal acceptance. Simulations have demonstrated that a high injection efficiency is achieved for bunch lengths under 5 mm. Moreover, significant energy oscillations during longitudinal injection, with peak energy deviations approaching 4%, reduce the transverse acceptance. Consequently, the horizontal geometric emittance must be kept below 20 nm rad. For standard longitudinal injection, the bunch charge needs to exceed 0.25 nC, identified as the normal-charge (norm-Q_c) mode. Once the storage ring is activated, the injection process, escalating from zero to full beam current, is projected to take less than a minute, thereby enhancing light source utilization. In this mode, each bucket in the ring is filled with a single injected bunch, demanding a bunch charge of 4.2 nC with an injection efficiency of 80%. This state of operation is labeled as the high-charge (high-Q_c) mode.

As demonstrated by Eqs. (1) and (2), minimizing emittance and bunch length can be achieved by increasing the ring circumference and reducing α_p. One approach to reduce α_p is the use of combined-function magnets. Optimization algorithms [54, 55] were employed to design these lattices. To facilitate the selection of the optimal lattice structures, we conducted a comparative analysis. The main parameters of these lattices are summarized in Table 2, which includes a FODO structure with an increased circumference, a modified TME structure and a structure incorporating full combined-function magnets. To meet the injection requirements, the circumference of the FODO structure must be increased to approximately 380 m, significantly enlarging the accelerator and substantially increasing costs. Under the condition of equal circumference, the key parameters of the TME structure are similar to those of the full combined-function magnet structure. However, during the design process, it was found that optimizing the nonlinear dynamics of full combined-function magnets is particularly complicated and demands a higher tolerance for magnet errors. Considering both the costs and operational reliability, the modified TME structure was ultimately selected.

Table 1 The beam requirements for SAPS injection

Parameters	Values
Horizontal emittance, ϵ_x (nm rad)	< 20
Vertical emittance, ϵ_y (nm rad)	< 4
Bunch length (σ) (mm)	< 5
Beam energy (GeV)	3.5
Repetition rate (Hz)	2
Bunches per pulse	4
Bunch charge of norm-Q_c mode (nC)	> 0.25
Bunch charge of high-Q_c mode (nC)	> 4.2

Figure 2 displays the layout of a booster-based injector. The booster synchrotron-based injector for the SAPS consists of a 250 MeV linac, a booster synchrotron that accelerates the beams to a full energy of 3.5 GeV for storage in the ring, and two transport lines. The remainder of this paper is organized as follows: Sect. 2 describes the preliminary design of the linac, outlining the components and their functions. Section 3 elaborates on the lattice design and beam parameters of the booster synchrotron, closed orbit correction, longitudinal dynamics design and high-intensity study. Section 4 presents the design of the beam transport lines, and booster injection and extraction, explaining their roles in beam delivery and manipulation. Section 5 introduces the simulation of the transmission efficiency from the electron gun to the injection point in the storage ring. Section 6 discusses the injector design for longitudinal injection scheme.

Table 2 Key parameter comparison of optional lattices

Parameters	FODO	TME	Combined type
Circumference (m)	379.8	257.39	257.39
Emittance (nm rad)	5.6	1.66	1.6
Bunch length, σ (mm)	4.7	4.6	4.5

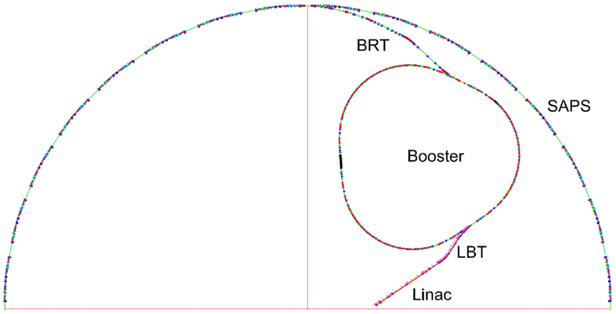

Fig. 2 (Color online) Layout of SAPS booster-based injector

The concluding section summarizes the findings and proposals, highlighting the advancements of the SAPS project.

2 Linac design

The 250 MeV linac functions as the pre-injector for the synchrotron light source, delivering electron bunches to the booster synchrotron. The layout of the pre-injector [56] is illustrated in Fig. 3. The system comprises three sections: a DC electron gun, a bunching section and an accelerating section that includes four S-band accelerating cavities.

As a user facility, the linac should be operated with high reliability, which is challenging when employing an RF photocathode gun equipped with a semiconductor cathode for high bunch charge. Therefore, a thermionic high-voltage DC gun is chosen, capable of providing the required bunch charge to the booster. The total capture efficiency is assumed to be 80%; therefore, this DC gun must provide electron bunches with a charge of 6.5 nC. The software EGUN [57] is utilized for the DC gun design. The full-width at half-maximum (FWHM) bunch length is 1.1 ns. For the normal-charge mode, this gun can also provide bunches with low bunch charge by adjusting the bias voltage.

The bunching system compresses the bunch into a single bunch, comprising two subharmonic cavities, a standing-wave S-band pre-buncher, a traveling-wave S-band buncher and a standard S-band cavity. After passing through this bunching system, over 90% of electrons are of 10 ps, ensuring low-energy spread acceleration in the subsequent linac. The entire system is encased in a solenoid focusing channel for transverse focusing and emittance preservation. Our design incorporates 23 solenoids, each with a maximum magnetic field of 0.1 T. The final traveling-wave cavity not only compresses the electron bunch but also provides beam acceleration. The bunch energy after this section is approximately 50 MeV.

The accelerating system comprises four traveling-wave S-band accelerating cavities to increase the bunch energy from 50 MeV to 250 MeV. Two adjacent cavities are grouped together and powered by a klystron. The microwave from the klystron is compressed using SLAC Energy Doubler (SLED) technology [58] to achieve high peak power. The average accelerating gradient of the linac can exceed 20 MV/m. Along the linac cavities, three quadrupole triplets are used to match and focus the beam. The wakefield in the S-band linac is also estimated, and BNS damping [59] is employed to mitigate its effects.

The linac operates in two distinct charge modes: a standard-charge mode dedicated to longitudinal injection into the storage ring and a high-charge mode optimized for fast beam accumulation from zero to full current upon storage ring activation. The high-charge mode presents notable challenges for the linac, prompting a focused design approach. Alignment errors for all components are assumed to possess RMS standard deviations of 0.1 mm and 0.1 mrad, while cavities and magnets are presumed to exhibit field errors of 0.1%. Following error assessment and correction, optimization and comparison tasks were performed using the ELEGANT [60] and ASTRA [61] codes, with the main beam parameters detailed in Table 3. Ultimately, the beam energy was found to reach 250 MeV. The linac achieved a transmission efficiency exceeding 95%, accompanied by normalized emittances of approximately 60 mm mrad in the transverse plane. A bunch charge of 5.2 nC is required for a booster with an 80% transmission efficiency. The transition from the high-charge mode to the normal-charge mode can be seamlessly accomplished by adjusting the settings of the electron gun, solenoids and cavities. In this context, the beam emittance and spread are diminished compared to the

Table 3 Main beam parameters at linac end

Parameters	High-Q_c mode	Norm-Q_c mode
Energy (MeV)	250	250
Bunch charge (nC)	5.2	0.4
Norm. ϵ_x (mm mrad)	60	40
Norm. ϵ_y (mm mrad)	57	40
Beam spread (%)	0.4	0.24
Charge transmission (%)	> 90	> 90
Repetition rate (Hz)	50	50

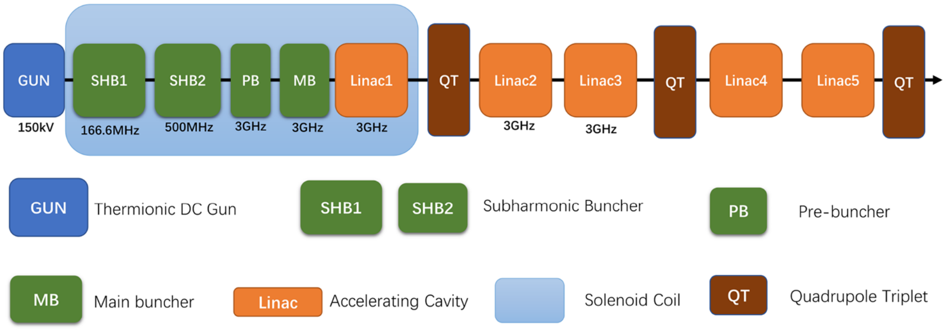

Fig. 3 (Color online) Layout of the linac accelerator

high-charge mode, thereby enhancing injector performance. Nonetheless, a bunch charge of 0.4 nC is maintained with the same transmission efficiency as in the high-charge mode.

3 Booster synchrotron

3.1 Booster lattice

The separate tunnel booster features a threefold structure, with each super-period consisting of 12 modified TME cells and two matching cells. The layout and optical functions of one period are depicted in Fig. 4. The modified TME cell comprises a combined-function dipole magnet and a set of quadrupole magnets. The matching cell, composed of two dipole magnets and powered by five separate power supplies for the quadrupoles, provides flexibility in optimizing the lattice. The lattice includes three long (7.3 m) straight sections with zero dispersion for the installation of RF cavities, as well as injection and extraction components. The main parameters of the booster are listed in Table 4. The circumference is reduced to 237 m, comprising 54 dipole magnets, 108 quadrupole magnets and 51 sextupole magnets. The lattice achieves a sufficiently low horizontal emittance of 3.98 nm rad at extraction, which is comparable to that of the third-generation storage ring. The bunch length is attained through a small α_p of 1.75×10^{-3} and a high voltage of 7.5 MV. The design with low emittance and short bunch length necessitates strong focusing field, leading to a significantly large natural chromaticity. Furthermore, the peak value of the dispersion is below 0.2 m. Consequently, a sextupole field for chromaticity correction is integrated into the combined-function dipoles to decrease the number of sextupole magnets.

Given the beam parameters for the pre-injector described in Sect. 2, the transverse beam sizes are (1.7 mm × 1.5 mm), respectively. It is assumed that the magnet aperture should be no less than 10 times the beam sizes. In the booster, the maximum strength of dipole magnets is approximately 1 T, with a defocusing strength of 0.542 T/m and a sextupole strength of 5.63 T/m^2. Three types of quadrupole magnets are utilized, with a maximum pole-face strength of 0.72 T. Additionally, one type of sextupole magnet is employed with a maximum pole-face strength of 0.6 T and a length of 0.15 m.

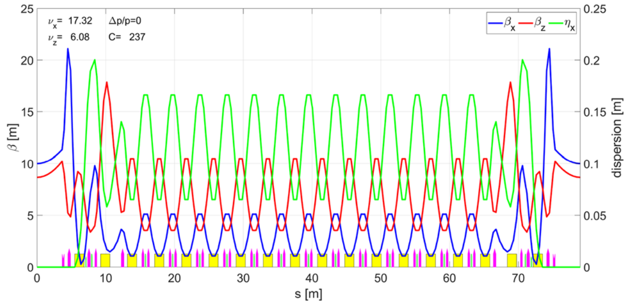

Fig. 4 (Color online) Twiss functions of one-third of the SAPS booster lattice. Blue, red and green curves represent the horizontal and vertical beta functions and the dispersion function. Yellow, pink and green blocks on the bottom correspond to the dipole, quadrupole and sextupole magnets, respectively

Table 4 Main parameters of booster lattice

Parameters	Value
Injection energy (GeV)	0.25
Extraction energy (GeV)	3.5
Circumference (m)	237
Natural emittance (nm rad)	3.98
Tune (*x*/*y*)	17.32/6.08
Natural chromaticity (*x*/*y*)	−26/−16.2
Momentum compact factor (10^{-3})	1.75
Damping time (*x*/*y*/*z*) (ms)	3.1/6.6/7.6
Energy loss per turn (MeV)	1.14
Maximum beta function (*x*/*y*) (m)	22/18
Maximum dispersion (m)	0.2
Harmonic number	395
Bunch number	4
Maximum beam current (mA)	21
Bunch length at extraction (mm)	4.8

In addition to the integrated sextupole component in the combined-function magnets, a family of sextupoles distributed in each TME cell is employed for chromaticity correction. Two additional families of sextupoles in the matching cells are utilized to minimize nonlinear driving terms. Independent power supplies for the sextupoles allow for separate adjustments of horizontal and vertical chromaticity. Using a 6D code to track particles for 1024 turns to obtain the dynamic aperture and corresponding frequency map. The sextupole strengths are optimized to achieve a large enough dynamic aperture. The optimized dynamic aperture and frequency map are shown in Fig. 5. The results indicate that the dynamic aperture approximates 15 mm.

3.2 Tolerance and correction

The ring is equipped with 54 BPMs for closed orbit correction, with one BPM positioned in each modified TME cell. It also has 73 dipole correctors, allocated as 38 for the horizontal plane and 35 for the vertical plane. The corrector fields are capable of tracking the energy ramp, ensuring orbit correction at all energy levels.

Preliminary evaluations encompass the magnet tolerances and the orbit correction system. Table 5 outlines the assumed RMS tolerances for magnet alignment and

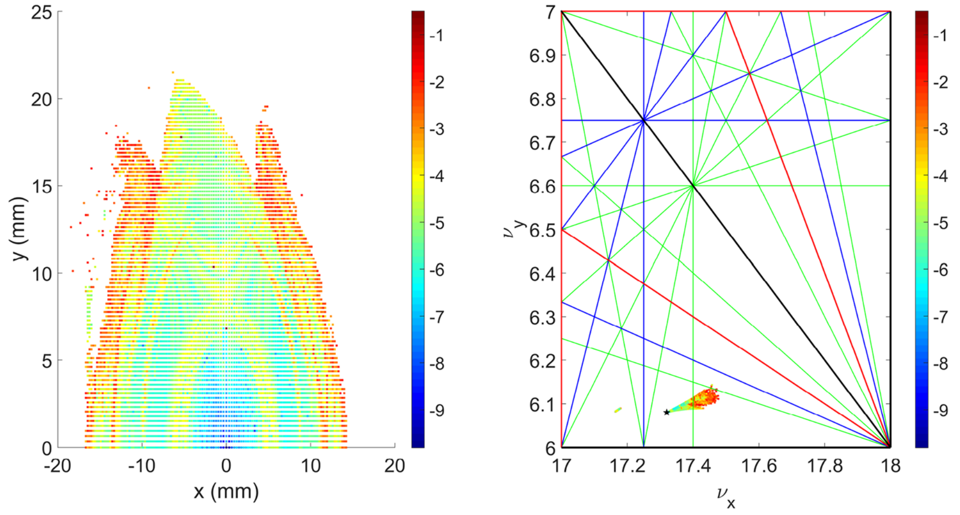

Fig. 5 (Color online) The dynamic aperture (left) and the frequency map (right) of the booster lattice on momentum particles

Table 5 Magnet tolerances

Source of error	Value
Dipole angle (%)	0.25
Dipole transverse misalignment (mm)	0.1
Dipole longitudinal misalignment (mm)	0.2
Dipole roll (mrad)	0.2
Quadrupole transverse misalignment (mm)	0.075
Quadrupole longitudinal misalignment (mm)	0.2
Quadrupole gradient (relative) (%)	0.2
Quadrupole roll (mrad)	0.2
Sextupole transverse misalignment (mm)	0.1
Sextupole longitudinal misalignment (mm)	0.2

fields. Another significant source of closed orbit distortion is the stray field from the extraction Lambertson magnet operating in DC mode, which significantly impacts the circulating beam, especially at low-energy stages. A local bump has been designed to mitigate this distortion. Tolerances on the magnet parameters are developed using analytical estimates, assuming Gaussian type of random errors in all magnets. In the orbit correction simulations, 1000 sets of random seeds are generated. With these BPMs and correctors, the closed orbit distortion due to errors listed in Table 5 can be effectively corrected. The BPM-corrector configuration makes sure that the orbit will be with a maximum deviation of 1.5 mm in each plane after correction, as shown in Fig. 6, with average RMS values of 0.23 mm and 0.2 mm in horizontal and vertical plane, respectively. This requires a maximum corrector strength of 0.5 mrad, simplifying the magnet design and fabrication. Furthermore, based on orbit correction, an analysis is conducted to evaluate the impact of magnet alignment errors and field errors on the dynamic aperture. Considering the errors specified in Table 5, the dynamic aperture is reduced to 12 mm, yet it still met the dynamic aperture requirements for both charge modes.

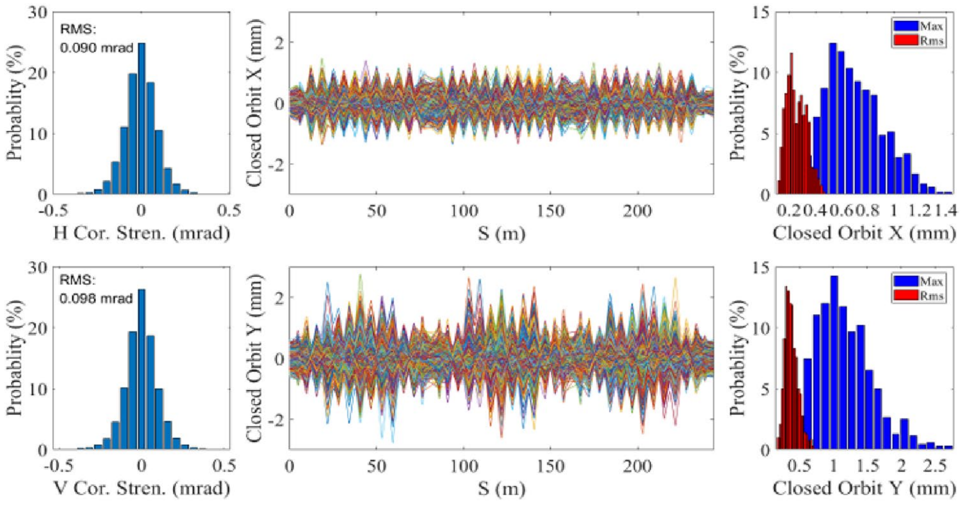

Fig. 6 (Color online) The closed orbit distortion of the booster lattice after correction

During operation, the dynamic errors of the power supply are characterized by stability, repeatability and ripples. To investigate the perturbations in the tune, simulations are performed using the ELEGANT code [60]. In these simulations, the total dynamic error for each magnet is modeled using a random 3σ truncated Gaussian distribution. Various RMS error values are scanned, generating 2000 sets of random error seeds for each condition. When the error value is below 4×10^{-4}, the tune avoids major resonance lines and maintains high transmission efficiency, thus informing power supply design.

3.3 Longitudinal beam dynamics

The ramp cycle consists of a 60-ms flat bottom for accumulating the injected beam at the beginning, a ramping curve for acceleration, an equally long flat top for extracting the accelerated beam and a ramping-down. Reference [62] discusses the impact of various ramping curves on emittance. Given the 60-ms flat top and enhanced ramping accuracy, a comparable sinusoidal curve of energy $E(t)$ is utilized over a duration of 220 ms

$$E(t) = 1.875 + 1.625\sin(2\pi f t), \tag{3}$$

with $f \approx 2.2727$ Hz and ramping time t. The ramping curve and the beam evolution in the booster are depicted in Fig. 7. The beam energy increases from 250 MeV to 3.5 GeV in 220 ms. The RF voltage is set to 2 MV at injection and 7.5 MV at extraction. The synchrotron tune shifts from 0.026 at injection to 0.015 at extraction, while the bucket height reduces from 7% to 4%. The evolution of beam energy spread and emittance with energy ramping is detailed in Ref. [63] as

$$\frac{\mathrm{d}A_i}{\mathrm{d}t} = -A_i\left(\frac{\dot{E}}{E} + J_i\frac{P_\gamma}{E}\right) + C_q\frac{P_\gamma\gamma^2}{E}G_i \tag{4}$$

with $i = 1$ and 2. For $i = 1$, A_1 denotes the energy spread; J_1 is the longitudinal damping partition and $G_1 = I_3/I_2$ with the synchrotron radiation integration I_2 and I_3. For $i = 2$, A_2 represents horizontal emittance ϵ_x, J_2 is the horizontal damping partition J_x and $G_2 = I_5/I_2$ with the synchrotron radiation integration I_5. $\dot{E}$ is the energy slope at energy E with the relativistic energy factor γ. P_γ is the synchrotron radiation power. When the energy exceeds 2.5 GeV, the emittance and energy spread attain equilibrium as a result of radiation damping and quantum excitation.

Additionally, the induced eddy current in the dipole vacuum chamber produces an extra sextupole field. The induced sextupole strength during ramping [64, 65] is calculated as

$$B_2 = 2F\mu_0\sigma\frac{h}{g}\frac{\mathrm{d}B}{\mathrm{d}t}, \tag{5}$$

where σ is the conductivity; h and g are the thickness and height of the vacuum chamber, respectively. F is the form factor of chamber, and μ_0 is the magnetic permeability of vacuum. For the specified lattice parameters, the estimated maximum field of the sextupole is 0.3 T/m^3 at a repetition rate of 2 Hz. The corresponding chromaticity values are approximately 1.7 for horizontal plane and −1.3 for vertical plane, which are significantly smaller than the natural chromaticity and can be easily compensated by ramping up sextupoles.

3.4 Estimation of beam effects due to high intensity

The SAPS is in the design phase, making the development of an accurate impedance model challenging. However, key components contributing to the impedance can be inferred from other existing accelerators. In this study, we construct a vertical impedance Z_v, as depicted on the left side of Fig. 8, by scaling the impedance of the HEPS booster [66, 67] as

$$Z_\mathrm{v} = \frac{Z_\mathrm{HB}C}{C_\mathrm{HB}} + N_\mathrm{c}Z_\mathrm{HOM}, \tag{6}$$

where C_HB represents the circumference of the HEPS booster [51] and the number of cavities $N_\mathrm{c} = 5$. A 5-cell copper cavity will be employed, serving as the source of the higher-order modes (HOM, Z_HOM) observed in the impedance spectrum. Z_HB refers to the HEPS booster impedance excluding the cavity impedance.

Instabilities commonly observed in other accelerators [68, 69] are estimated for the booster. For the high-charge mode, the beam current in the booster is approximately 20 mA.

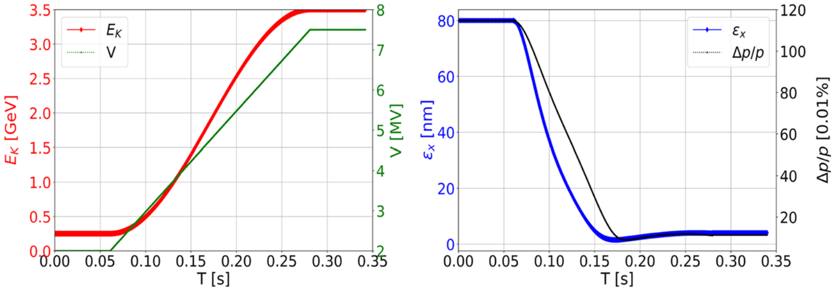

Fig. 7 (Color online) Ramping curve (left) and beam energy spread and emittance evolution with energy ramping

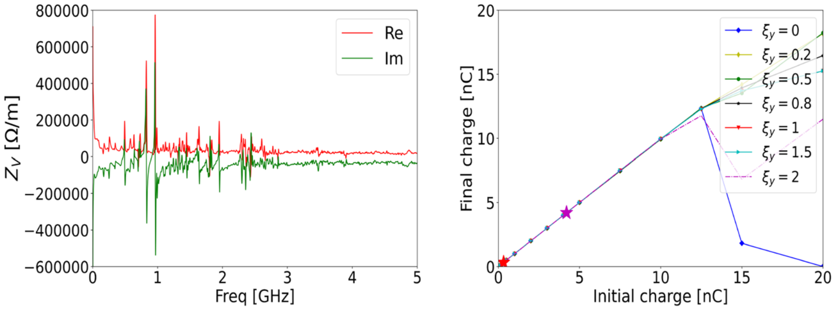

Fig. 8 (Color online) Impedance model in the booster (left) and living charge in terms of chromaticity (right)

The growth time $1/\tau$ of transverse coupled-bunch instability (TCBI), driven by HOMs, is expressed [70] as

$$\frac{1}{\tau} = \frac{1}{N_c} \frac{2E}{f_{\mathrm{rev}} I_b \beta Z_{\mathrm{HOM}}}, \tag{7}$$

where I_b is average beam current with revolution frequency f_{rev}, and β is beta function at the cavity. The growth time in the vertical plane is calculated to be 0.78 ms at injection and 11 ms at extraction. These results indicate that the TCBI growth time at extraction energy exceeds the damping time of 6.3 ms; thereby, the instability can be suppressed. Conversely, the beam remains unstable at injection due to the excessively long damping time. Consequently, a transverse feedback system with a damping time of 0.5 ms is proposed.

Single-bunch effects are simulated utilizing the ELEGANT code [60] for the bare lattice, with the threshold charges depicted in the right side of Fig. 8. The heat-tail instability is observed at high bunch charges in the simulation. As head-tail effects emerge, both the oscillations amplitude of beam position and the vertical emittance increase. Nevertheless, the results show that the instability threshold charge is around 15 nC, which is substantially higher than the required charge of 4.2 nC for the high-charge mode. Furthermore, a longitudinal impedance model is also developed to investigate the dependence of bunch length on bunch charge. The findings reveal that the bunch length increases significantly due to microwave instability when the charge exceeds 20 nC. Consequently, bunch lengthening is expected to be negligible in both normal-charge and high-charge modes.

4 Beam transport lines and booster injection, extraction

These references [71–73] serve as the basis for the design considerations of this section. The linac-to-booster transport line (LBT) serves as the beam line connecting the linac to the booster. The transfer line must fulfill several functions: beam matching between the linac and booster, and providing space for beam diagnostic elements and momentum collimators. The high-charge mode is considered in the design. The transfer line consists of two doublet bend achromat (DBA) structures, ensuring a dispersion-free condition. It includes 3 dipoles and 12 quadrupoles, with all dipole magnet angles set at 200 mrad. Instrumentation elements are arranged along the 24.4 m transfer line. The maximum beta function is 35 m with maximum dispersions of 0.6 m. The horizontal collimator is positioned in the first DBA structure with a transverse aperture of 16 mm, effectively reducing the energy spread to the required level. The RMS energy spread after collimation is 0.36%. Error studies show that beam emittance does not significantly increase along the transfer line, and beam loss is mainly confined to the collimation section. The booster injection system is situated in one of the two remaining dispersion-free straight section and comprises a DC Lambertson magnet and a kicker. It utilizes single-turn on-axis injection, enabling the injection of one bunch into the booster RF buckets. The Lambertson has a bend angle of 200 mrad in the horizontal plane, while the kicker has a bend angle of 6.5 mrad in the vertical plane.

The booster extraction system is located in the last dispersion-free straight sections and comprises four slow orbit bumpers, a Lambertson magnet and a kicker. The slow bumpers incrementally shift the orbit of the circulating bunch train toward the extraction Lambertson over several hundred turns. Following this, the extraction kicker directs one bunch into the extraction Lambertson at a vertical angle of zero. The kicker strength is 1.2 mrad, while the Lambertson kick angle is set at 100 mrad. Two of the four bump magnets are positioned in the matching cell, with a maximum bumper strength of 1.3 mrad. Simulations confirm the design, achieving 100% extraction efficiency. Additionally, the beam, carrying a charge of 5 nC, is tracked from injection to extraction in the booster, with the primary results shown in Fig. 9. The injected beam quickly reaches equilibrium after injection in the booster. During the injection plateau phase, these parameters show minimal change, while in the acceleration phase, they gradually stabilize and reach equilibrium values. This outcome indicates high beam performance throughout the booster.

The Booster-to-Ring Transport line (BRT) is designed to efficiently convey the booster beam into the storage ring.

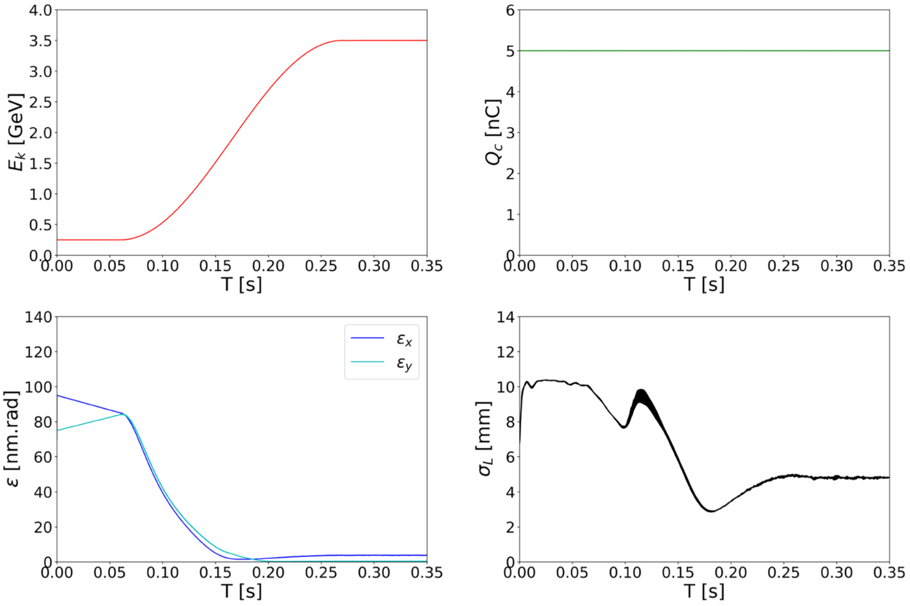

Fig. 9 (Color online) Trace simulations of beam parameter from injection to extraction in the booster, including the energy, charge, emittance and bunch length

Due to the low vertical emittance, the beam is vertically injected into the ring to minimize the kick intensity in the storage ring. The BRT consists of 12 dipoles and 19 quadrupoles, extending over a length of 60 m. This transport line is functionally divided into three segments: the extraction matching section, the dispersion-free section and the injection matching section. The dispersion-free section is allocated for the installation of beam diagnostic elements. The magnet aperture is less than 30 mm. The beam transmission efficiency in the BRT is approximately 99%.

5 Transmission efficiency simulation

After completing the physical design of the injector, we have studied the overall transmission efficiency. Transmission efficiency is defined as the ratio of the charge captured by the storage ring to the charge output from the electron gun. The start-to-end simulation is systematically executed to ensure that the input parameters at each accelerator stage precisely matched the output parameters of the preceding stage, facilitating a seamless acceleration and transmission process. The simulation rigorously tracks the beam from its generation at the electron gun through the linac, the LBT, injection, acceleration, and extraction in the booster, and the BRT, ultimately leading to injection point in the storage ring. Realistic error margins expected at each accelerator stage are incorporated into the simulation. To evaluate overall performance, we generate 100 random seeds and perform a comprehensive statistical analysis of the transmission efficiency and the charge accumulated in the storage ring.

First, the high-charge mode is simulated. The results demonstrate exceptional efficiency, with an average transmission efficiency approaching 90%, and most beam loss occurring at the collimator in the LBT. Furthermore, across all simulation scenarios, the accumulated charge in the storage ring exceeded the required charge of 3.33 nC. This indicates that our injector design meets the criteria for efficient injection, even when realistic operational errors are considered. To further validate the robustness of the injector design, equivalent simulation studies are performed for the normal-charge mode. Encouragingly, in this mode, the transmission efficiency exceeds 90% in every case, providing additional evidence of the design's efficiency and reliability.

6 Discussion

The synchrotron radiation light sources are undergoing rapid development globally. The selection of an injector with high stability, high beam quality, robustness and cost-effectiveness at the same time is crucial to advance the synchrotron radiation light sources. Presently, synchrotron radiation light sources are categorized as high-, medium- and low-energy sources based on their beam energies. High-energy light sources, exemplified by the HEPS [14], operate at energies exceeding 6 GeV and favor booster-based injector schemes for efficient cost management. Low-energy light sources, with energies below 2.5 GeV, can accommodate a full-energy linac injector due to their lower energy requirements, as illustrated by the HALF [15]. Medium-energy light sources fall between these extremes and necessitate a thorough consideration of various injector options. For instance, the SAPS has assessed multiple injector schemes, including full-energy linac, booster-based injection and innovative injectors, to align with technical requirements, costs and expansion applications in the future. Despite the availability of innovative injector schemes and technologies, such as laser plasma accelerators, these alternatives often introduce heightened risks for operation. Recent studies have shown that booster-based injectors offer significant advantages over other injector types.

The longitudinal injection design of the SAPS imposes requirements on the beam with high quality of the injector, especially concerning the bunch length and beam emittance. It is crucial for achieving the desired bunch length and emittance while keeping the booster size reasonable. One strategy involves increasing the voltage. To attain the required beam quality, the voltage must be increased by an order of magnitude, necessitating sufficient space for RF cavity installation. Another method entails compressing α_p, which necessitates strong focusing fields, reducing the dynamic aperture and tightening magnet error tolerances. These challenges escalate not only the cost of the injector but also the construction risks, potentially undermining the advantages of a booster-based injector. Balancing these factors, a hybrid approach has been adopted, combining α_p compression and voltage augmentation to preserve the benefits of the booster-based injector. The booster injector offers a promising solution for the longitudinal injection scheme of the DLSR storage ring. Considering the limitations of authors, such as simulation assumptions, and the incorporation of more practical parameters in subsequent optimizations, future work will focus on optimizing design parameters, enhancing system stability and preparing for the actual construction stages. Nevertheless, the successful beam commissioning from the HEPS injector [74, 75] offers substantial encouragement for its ongoing success.

7 Summary

A beam with a short bunch length and low emittance is vital for the storage ring injection of SAPS. This paper presents a detailed overview of the physical design of a booster-based injector engineered to meet these requirements. The injector system comprises a linac, a booster synchrotron and two beam transport lines. The booster synchrotron accelerates electron beams from 250 MeV to 3.5 GeV at a repetition rate of 2 Hz. The lattice of the booster synchrotron consists of 54 dipole magnets, 108 quadrupole magnets, and 51 sextupole magnets. The required beam parameters for SAPS injection are achieved by employing a modified TME structure with a small momentum compaction factor and a high RF voltage. The resulting beam emittance is 3.98 nm rad with a bunch length of 4.8 mm. Simulation studies of beam transmission efficiency indicate an overall efficiency of about 90%. Detailed analysis of beam collective effects, based on the current impedance model, shows that the charge stored in the injector significantly exceeds the SAPS injection requirement. These findings confirm that the injector meets the injection requirements of the SAPS storage ring. The theoretical and simulation studies of the injector design demonstrate outstanding performance.

Acknowledgements The authors would like to thank Yuemei Peng, Cai Meng, Haisheng Xu and Saike Tian for their fruitful discussions and data support. We are also grateful to colleagues from the power supply and magnet groups for their discussions.

Author Contributions All authors contributed to the study conception and design. Material preparation, data collection and analysis were performed by Liang-Sheng Huang, Yan-Liang Han, Wei-Hang Liu, Jian-Liang Chen. The first draft of the manuscript was written by Liang-Sheng Huang and Yan-Liang Han, and all authors commented on previous versions of the manuscript. All authors read and approved the final manuscript.

Data Availability The data that support the findings of this study are openly available in Science Data Bank at https://cstr.cn/31253.11.sciencedb.10732 and https://www.doi.org/10.57760/sciencedb.10732.

Declarations

Conflict of interest Yi Jiao is an editorial board member for Nuclear Science and Techniques and was not involved in the editorial review or the decision to publish this article. All authors declare that there is no conflict of interest.

References

1. M. Magnuson, M. Fahlman, R. Uhrberg et al., *MAX IV conceptual design report* (Rep. CDR, Max IV, Lund, Sweden, 2006)
2. P. Tavares, S. Leemann, M. Sjöström et al., The MAX IV storage ring project. J. Synchrotron Radiat. **21**, 862–877 (2014). https://doi.org/10.1107/S1600577514011503
3. C. Schroer, I. Agapov, W. Brefeld et al., BPETRA IV: the ultralow-emittance source project at DESY. J. Synchrotron Radiat. **25**, 1277–1290 (2018). https://doi.org/10.1107/S1600577518008858
4. P. Goslawski, M. Abo-bakr, F. Andreas et al., BESSY III & MLS II–status of the development of the new photon science facility in Berlin, in *Proc. of IPAC'12, Campinas, Brazil, MOPAB126* (2021), pp. 451–454. https://doi.org/10.18429/JACoW-IPAC2021-MOPAB126
5. Conceptual Design Report for SOLEIL Upgrade, (2021). www.synchrotron-soleil.fr
6. A. Streun, T. Garvey, L. Rivkin et al., SLS-2—the upgrade of the Swiss light source. J. Synchrotron Radiat. **25**, 631–641 (2018). https://doi.org/10.1107/S1600577518002722
7. E. Karantzoulis, A. Fabris, S. Krecic, The ELETTRA 2.0 project, in *Proc. of IPAC'22, Bangkok, Thailand, TUPOMS023*, (2022), pp. 1459–1462. https://doi.org/10.18429/JACoW-IPAC2022-TUPOMS023
8. C. Steier, A. Allezy, A. Anders et al., Status of the conceptual design of ALS-U. in *Proc. of IPAC'17, Copenhagen, Denmark, WEPAB104*, (2017), pp. 2824–2826
9. L. Liu, N. Milas, A. Mukai et al., The Sirius project. J. Synchrotron Radiat. **21**, 904–911 (2014). https://doi.org/10.1107/S1600577514011928

10. SPring-8-II Conceptual Design Report. RIKEN SPring-8 Center, (2014). https://docslib.org/doc/4975580/spring-8-ii-conceptual-design-report
11. G.S. Jang, S. Shin, M. Yoon et al., Low emittance lattice design for Korea-4GSR. Nucl. Instrum. Methods Phys. Res. A **1034**, 166779 (2022). https://doi.org/10.1016/j.nima.2022.166779
12. P. Raimondi, N. Carmignani, L. Carver et al., Commissioning of the hybrid multibend achromat lattice at the European synchrotron radiation facility. Phys. Rev. Accel. Beams **24**, 110701 (2021). https://doi.org/10.1103/PhysRevAccelBeams.24.110701
13. T.E. Fornek, Advanced photon source upgrade project final design report. Argonne National Laboratory, United States, (2019). https://doi.org/10.2172/1543138
14. Y. Jiao, G. Xu, X. Cui et al., The HEPS project. J. Synchrotron Radiat. **25**, 1611–1618 (2018). https://doi.org/10.1107/S1600577518012110
15. Z.H. Bai, G.W. Liu, T.L. He et al., Preliminary physics design of the Hefei Advanced Light Facility storage ring. High Power Laser Part. Beams **34**, 104003 (2022). https://doi.org/10.11884/HPLPB202234.220137. (**in Chinese**)
16. D. Einfeld, M. Plesko, J. Schaper, First multi-bend achromat lattice consideration. J. Synchrotron Radiat. **21**, 856–861 (2014). https://doi.org/10.1107/S160057751401193X
17. H. Takaki, N. Nakamura, Y. Kobayashi et al., Beam injection with a pulsed sextupole magnet in an electron storage ring. Phys. Rev. ST Accel. Beams **13**, 020705 (2010). https://doi.org/10.1103/PhysRevSTAB.13.020705
18. Y. Jiao, G. Xu, Pulsed sextupole injection for Beijing Advanced Photon Source with ultralow emittance. Chin. Phys. C **37**, 117005 (2013). https://doi.org/10.1088/1674-1137/37/11/117005
19. M. Borland, A super-bright storage ring alternative to an energy recovery linac. Nucl. Instrum. Methods Phys. Res. A **557**, 230 (2006). https://doi.org/10.1016/j.nima.2005.10.076
20. A. Xiao, M. Borland, C. Yao et al. On-axis injection scheme for ultra-low-emittance light sources, in *Proc. of NAPAC'13, Pasadena, CA*, (2013), pp. 1076–1078
21. C. Steier, A. Anders, T. Luo et al., On-axis swap-out injection R+D for ALS-U, in *Proc. of IPAC'17, Copenhagen, Denmark, WEPAB103* (2017), pp. 2821–2823
22. Z. Duan, J. Chen, Y. Guo et al., The swap-out injection scheme for the high energy photon source, in *Proc. of IPAC'18, Vancouver, BC, Canada, THPMF052*, (2018), pp. 4178–4181. https://doi.org/10.18429/JACoW-IPAC2018-THPMF052
23. M. Aiba, M. Boge, F. Marcellini et al., Longitudinal injection scheme using short pulse kicker for small aperture electron storage rings. Phys. Rev. ST Accel. Beams **18**, 020701 (2015). https://doi.org/10.1103/PhysRevSTAB.18.020701
24. M. Tordeux, R. Nagaoka, A. Chao et al., Longitudinal injection into low-emittance ring: a novel scheme for SOLEIL upgrade, in *Topical Workshop on Injection, Berlin* (2017), pp. 28–30
25. S. Jiang, G. Xu, On-axis injection scheme based on a triple-frequency RF system for diffraction-limited storage rings. Phys. Rev. Accel. Beams **21**, 110701 (2018). https://doi.org/10.1103/PhysRevAccelBeams.21.110701
26. J. Kim, G. Jang, M. Yoon et al., Injection scheme with deflecting cavity for a fourth-generation storage ring. Phys. Rev. Accel. Beams **22**, 011601 (2019). https://doi.org/10.1103/PhysRevAccelBeams.22.011601
27. L.C. Teng, Minimizing the emittance in designing the lattice of an electron storage ring. Fermilab Report TM-1269 (1984). https://doi.org/10.2172/6690255
28. S.Y. Lee, *Accelerator Physics*, 2nd edn. (World Scientific, Singapore, 2004), p.251
29. S. Wang, J. Chen, Y. Han, et al., Proposal of the Southern Advanced Photon Source and current physics design study, in *Proc of IPAC'21, Campinas, SP, Brazil, MOPAB075* (2021), pp. 300–303. https://doi.org/10.18429/JACoW-IPAC2021-MOPAB075
30. Y. Zhao, Y. Jiao, S. Wang, Design study of APS-U-type hybrid-MBA lattice for mid-energy DLSR. Nucl. Sci. Tech. **32**, 71 (2021). https://doi.org/10.1007/s41365-021-00902-1
31. Y. Zhao, Y. Jiao, Z. Li et al., Improving the MWI threshold of the modified hybrid-7BA lattice design for SAPS. Nucl. Instrum. Methods Phys. Res. A **1056**, 168565 (2023). https://doi.org/10.1016/j.nima.2023.168565
32. S. Wang, S. Fu, H. Qu et al., Design, Development and commissioning for high-intensity proton accelerator of China Spallation Neutron Source. Atom. Energy Sci. Technol. **56**, 1747–1759 (2022). https://doi.org/10.7538/yzk.2022.youxian.0591. (**in Chinese**)
33. W. Liu, Y. Jiao, Y. Zhao et al., Multi-objective optimization of longitudinal injection based on a multi-frequency RF system for fourth-generation storage ring-based light sources. Nucl. Instrum. Methods Phys. Res. A **1046**, 167712 (2023). https://doi.org/10.1016/j.nima.2022.167712
34. X. Liu, S. Jiang, W. Liu et al., Start-to-end simulation of the full energy linac injector for the Southern Advanced Photon Source, in *Proc. of IPAC'23, Venice, Italy. TUPL111* (2023), pp. 1992–1994. https://doi.org/10.18429/JACoW-IPAC2023-TUPL111
35. D. Li, H. Du, H. Li et al., Status of the SSRF booster, in *Proc. of EPAC'08, Genoa, Italy, WEPC083*, (2008), pp. 2089–2191
36. P. Raimondi, C. Benabderrahmane, P. Berkvens et al., The extremely brilliant source storage ring of the European Synchrotron Radiation Facility. Commun. Phys. **6**, 82 (2023). https://doi.org/10.1038/s42005-023-01195-z
37. S. V. Milton, The APS booster synchrotron: commissioning and operational experience, in *Proceedings Particle Accelerator Conference*, vol. 1 (Dallas, TX, USA, 1995), pp. 594–596. https://doi.org/10.1109/PAC.1995.504730
38. S. Gurov, S. Karnaev, V. Kiselev, et al., Commissioning of NSLS-II booster, in *Proc. of IPAC'14, Dresden, Germany, MOPRO088* (2014), pp. 295–297
39. F. H. Sa, L. Liu, X. Resende, et al., A new booster synchrotron for the SIRIUS project, in *Proc. of IPAC'14, Dresden, Germany, WEPRO009*, (2014), pp. 1959–1961. https://doi.org/10.18429/JACoW-IPAC2014-WEPRO009
40. A. Loulergue, M. Tordeux, A. Dael et al., The new booster synchrotron for SOLEIL, in *Proc. of EPAC'02, Paris, France* (2002), pp. 593–595
41. H.C. Chao, J.W. Tsai, H.P. Chang et al., Conceptual design of booster synchrotron for TPS, in *Proc. of EPAC'08, Genoa, Italy, THPC005*, (2008), pp. 2981–2983
42. G. Benedetti, D. Einfeld, Z. Marti, et al., Optics for the ALBA booster synchrotron, in *Proc. of EPAC'08, Genoa, Italy, WEPC067*, (2008), pp. 2148–2150
43. C.H. Kim, Commissioning experiences of the ALS booster synchrotron, in *Conference Record of the 1991 IEEE Particle Accelerator Conference*, vol. 5 (San Francisco, CA, USA, 1991), pp. 2691–2693. https://doi.org/10.1109/PAC.1991.165073
44. D. Scott, J. Clarke, D. Dykes et al., A revised DIAMOND booster design, in *Proc. of EPAC'02, Paris, France*, (2002), pp. 617–619
45. G. Zanyan, B. Grigoryan, K. Manukyan et al., Low emittance booster design for CANDLE storage ring. in *Proc. of IPAC'11, San Sebastián, Spain, THPC137*, (2011), pp. 3209–3211
46. A. Fabris, P. Craievich, C. Pasotti et al., RF system for the ELETTRA booster synchrotron, in *Proc. of EPAC'00, Vienna, Austria*, (2000), pp. 1957–1959
47. H.C. Chao, I.V. Agapov, S.A. Antipov, Design considerations of a high intensity booster for PETRA IV, in *Proc. of IPAC'21, Campinas, SP, Brazi, TUPAB023*, (2021), pp. 1386–1389. https://doi.org/10.18429/JACoW-IPAC2021-TUPAB023

48. M. Tordeux, A. Loulergue, R. Nagaoka et al., A low-emittance booster lattice design for the SOLEIL upgrade, in *Proc. of IPAC'21, Campinas, SP, Brazi, MOPAB113*, (2021), pp. 410–413. https://doi.org/10.18429/JACoW-IPAC2021-MOPAB113
49. Y. M. Peng, Y. Jiao, G. Xu et al., Candidate booster design for the HEPS project, in *Proc. of IPAC'16, Busan, Korea, THPMB018*, (2016), pp. 3263–3265
50. Y. M. Peng, Z. Duan, Y.Y. Guo et al., The progress of HEPS booster design, in *Proc. of IPAC'17, Copenhagen, Denmark, TUPAB065* (2017), pp. 1472–1474. https://doi.org/10.18429/JACoW-IPAC2018-TUPMF062
51. Y. M. Peng, Z. Duan, Y.Y. Guo et al., Status of HEPS booster lattice design and physics studies, in *Proc. of IPAC'18, Vancouver, BC, Canada, TUPMF06* (2018), pp. 1407–1410. https://doi.org/10.18429/JACoW-IPAC2018-TUPMF062
52. C. Meng, X. He, Y. Jiao et al., Physics design of the HEPS LINAC. Radiat. Detect. Technol. Meth. **4**, 497–506 (2020). https://doi.org/10.1007/s41605-020-00205-w
53. W. Liu, injector parameter requirements for SAPS. SAPS Technical Note SAPS-AC-AP-TN-2023-003, (2023)
54. L. Yang, D. Robin, F. Sannibale et al., Global optimization of an accelerator lattice using multi-objective genetic algorithms. Nucl. Instrum. Methods Phys. Res. A **609**, 50–57 (2009). https://doi.org/10.1016/j.nima.2009.08.027
55. Y. Jiao, G. Xu, Optimizing the lattice design of a diffraction-limited storage ring with a rational combination of particle swarm and genetic algorithms. Chinese Phys. C **41**, 027001 (2017). https://doi.org/10.1088/1674-1137/41/2/027001
56. Y. Han, L. Huang, X. Liu et al., Design of a 250 MeV linac injector system for the Southern Advanced Photon Source. J. Phys. Conf. Ser. **2687**, 032004 (2024). https://doi.org/10.1088/1742-6596/2687/3/032004
57. W. Herrmannsfeldt, EGUN - an electron optics and gun design program. SLAC-331, (1988) https://doi.org/10.1016/j.nima.2023.169074
58. Z. Farkas, H. Hoag, P. Wilson et al., SLED, a method of doubling SLAC's energy. SLAC-TN-73-15, (1974). https://api.semanticscholar.org/CorpusID:605827
59. V. Balakin, A. Novokhatsky, V. Smirnov, VLEPP: transverse beam dynamics. Conf. Proc. C **830811**, 119–120 (1983)
60. M. Borland, elegant: a flexible SDDS-compliant code for accelerator simulation. *Advanced Photon Source*, LS-287, (2000). https://doi.org/10.2172/761286
61. K. Flottmann, ASTRA User Manual, (2023). http://www.desy.de/ mpyflo
62. Y. Lee, E.S. Kim, J.G. Hwang et al., Beam dynamics in the booster synchrotron of Korea-4GSR project. Nucl. Instrum. Methods Phys. Res. A **1060**, 169074 (2024). https://doi.org/10.1016/j.nima.2023.169074
63. D. Edwards, M.J. Syfers, *An Introduction to the Physics of High Energy Accelerators* (Wiley, New York, 1993), pp.110–115
64. J. Bergstrom, L. Dallin, Effects of Eddy Current Induced Sextupole Moments in the Booster during Ramping. CLS Design Note - 3.2.69.2 Rev. 0, (2000)
65. Y. M. Peng, J.Y. Li, C. Meng et al., Study of the ramping process for HEPS booster, in *Proc. of IPAC'19, Melbourne, Australia, TUPGW052*, (2019), pp. 1521–1523. https://doi.org/10.18429/JACoW-IPAC2019-TUPGW052
66. H.S. Xu, J.Y. Xu, N. Wang, Influences of harmonic cavities on single-bunch instabilities in electron storage rings. Nucl. Sci. Tech. **32**, 98 (2021). https://doi.org/10.1007/s41365-021-00926-7
67. S.K. Tian, N. Wang, Booster impedance simulation of the High Energy Photon Source. HEPS Technical Note, IHEP-HEPS-AC-AP-TN-2020-022, 2020. https://irihep.ac.cn/handle/311005/289659
68. N. Wang, Z. Duan, H. S. Xu et al., Studies on collective instabilities in HEPS, in *Proc. of IPAC'17, Copenhagen, Denmark, THPAB030*, (2017), pp. 3763–3766
69. H.S. Xu, Y.M. Peng, N. Wang, Studies of transverse single-bunch instabilities in booster synchrotrons. Nucl. Instrum. Methods Phys. Res. A **940**, 313–319 (2019). https://doi.org/10.1016/j.nima.2019.06.048
70. F. Marhauser, E. Weihreter, D. M. Dykes et al., HOM damped 500MHz cavity design for 3rd generation SR sources, in *Proc. of PAC'01, Chicago, USA, MPPH033*, (2001), pp. 846–848
71. Y.M. Peng, Design study of high energy photon source low energy beam transport line. Atom. Energy Sci. Technol. **53**, 1702–1705 (2019). https://doi.org/10.7538/yzk.2019.youxian.0140. (**in Chinese**)
72. Y. Y. Guo, J. H. Chen, Z. Duan et al., The injection and extraction design of the booster for the HEPS projection, *in Proc. of IPAC'18, Vancouver, BC, Canada, TUPMF046*, (2018), pp. 1356–1358. https://doi.org/10.18429/JACoW-IPAC2018-TUPMF046
73. Y.Y. Guo, Y.Y. Wei, Y.M. Peng et al., The transfer line design for the HEPS project. Radiat. Detect. Technol. Meth. **4**, 440–447 (2019). https://doi.org/10.1007/s41605-020-00209-6
74. C. Meng, X. H. Cui, Z. Duan et al. Beam commissioning of the HEPS linac, in *Proc. of IPAC'23, Venice, Italy, TUPL126*, (2023), pp. 2023–2026. https://doi.org/10.18429/JACoW-IPAC-23-TUPL126
75. Y.-M. Peng, J.-S. Cao, J.-H. Chen et al., Milestone progress of the HEPS booster commissioning. Nucl. Sci. Tech. **35**, 16 (2024). https://doi.org/10.1007/s41365-024-01365-w